Piezo-optics of InP in the visible-ultraviolet range

D. Rönnow, P. Santos, and M. Cardona
Max-Planck-Institut für Festkörperforschung, Heisenbergstrasse 1, 70569 Stuttgart, Germany

E. Anastassakis
Department of Physics, National Technical University, Athens 15780, Greece

M. Kuball
Department of Physics, Brown University, Box 1843, Providence, Rhode Island 02912
(Received 11 September 1997)

The piezo-optical properties of InP above the fundamental gap have been investigated. Uniaxial stress was applied along the [001] and [111] crystal directions and spectroscopic ellipsometry was used to determine the piezo-optical coefficients P_{11}, P_{12}, and P_{44} in the energy range 1.6–5.5 eV at room temperature. Deformation potentials were determined for the E_1 and $E_1+\Delta_1$ transitions. Semiempirical tight-binding calculations of the piezo-optical coefficients and deformation potentials are in reasonable agreement with experiment. [S0163-1829(98)04008-9]

I. INTRODUCTION

The change in optical properties due to external stress, i.e., the piezo-optical properties of semiconductors, are, like the optical constants or dielectric functions themselves, fundamental material parameters, and contain information about the electronic structure. In particular, uniaxial stress, which reduces the crystal symmetry, is an excellent tool for investigating the electronic structure and the strain deformation potentials.[1,2] Piezo-optical effects also play an important role in Brillouin scattering,[3] in Raman scattering by folded acoustic phonons in multiple quantum wells,[4] and in strained layer superlattices.[5] A reliable database on piezo-optical properties is also desirable when an optical technique, such as reflectance difference spectroscopy, is used to monitor semiconductor growth processes,[6] and when designing optical modulators.[7]

The piezo-optical properties are most generally described by a fourth-rank tensor P_{ijkl}, which connects the second-rank dielectric tensor ε_{ij} to the second-rank stress tensor X_{kl}. The tensor ε_{ij} can also be related to the strain tensor η_{rs} through the photo-elastic tensor k_{ijrs}:

$$\Delta\varepsilon_{ij}=P_{ijkl}X_{kl}=k_{ijrs}\eta_{rs}. \tag{1.1}$$

The piezo-optical tensor P_{ijkl} and the photoelastic tensor k_{ijrs} are related through $P_{ijkl}=k_{ijrs}s_{rskl}$, where s_{rskl} are the compliances. The linear piezo-optical tensor P_{ijkl} can be represented by a 6×6 symmetric matrix with indices $m,n=1,\ldots,6$ ($i=j=1\rightarrow m=1$; $i=1,j=2\rightarrow m=6$ and index permutations), i.e., $P_{ijkl}=P_{jikl}=P_{ijlk}=P_{nm}$. There are several definitions of the tensors that describe the change in optical properties with stress or strain. Often, $\Delta\varepsilon_{ij}^{-1}$ is related to the stress X_{kl} or the strain η_{rs}, according to[8,9]

$$\Delta\varepsilon_{ij}^{-1}=\pi_{ijkl}X_{kl}=p_{ijrs}\eta_{rs}, \tag{1.2}$$

where π_{ijkl} is referred to as the piezo-optical and p_{ijrs} the elastooptical tensor, respectively. The compliances s_{rskl} give the relationship between π_{ijkl} and p_{ijrs}: $\pi_{ijkl}=p_{ijrs}s_{rskl}$. The relation between our definition of the piezo-optical tensor [Eq. (1.1)] and that of Nye[8] [Eq. (1.2)] is

$$P_{ijkl}=-\varepsilon^2\pi_{ijkl}. \tag{1.3}$$

The reason for us using the definition in Eq. (1.1) is that our experiment gives ε directly.

For cubic crystals belonging to the O, O_h, and T_d classes (432, $m3m$, and $\overline{4}3m$) only three piezo-optical coefficients are required, P_{11}, P_{12}, and P_{44}. The point group of InP is T_d ($\overline{4}3m$). For isomorphic materials, e.g., polycrystalline and amorphous materials, the number of independent piezo-optical coefficients is reduced to two, since $P_{11}-P_{12}=P_{44}$.

For semiconductors, the piezo-optical coefficients have mainly been determined below the fundamental gap E_0.[10–12] In this region, the material is transparent and the piezo-optical coefficients can be measured in a transmittance configuration. Above E_0, experimental methods based on a reflection configuration must be used. Here, the piezo-optical coefficients, like the dielectric function itself, are complex quantities. Experimental techniques that enable the simultaneous determination of real and imaginary parts are therefore desirable. Methods like piezoreflectance[13] and piezoelectroreflectance[14] have been used. Spectroscopic ellipsometry was used by Etchegoin and co-workers to determine the piezo-optical properties above E_0 for Ge,[15] GaAs,[16] and Si.[17] In the present work we have used the same method to determine the piezo-optical properties of InP above E_0.

For InP, the piezo-optical coefficients[10–12] and the stress-induced optical activity[18] have been determined below E_0. We believe, however, that our piezo-optical coefficients are the first to be reported for energies above E_0. Strain deformation potentials have been determined for the E_0 transition for uniaxial[10,12,19–21] and hydrostatic stress.[21–26] In the present work we determine the deformation potentials for the E_1-$E_1+\Delta_1$ transitions in InP. Earlier theoretical work has

been concerned with the deformation potentials for the E_0 transition under hydrostatic[27–34] and uniaxial stress,[28,33] and also those of the E_1 transition under hydrostatic stress.[27,29–32]

The outline of the paper is as follows. In Sec. II, experimental details are given, while the results are presented in Sec. III. The dielectric function obtained at various stresses is presented in Sec. III A. These experimental data are used to determine the piezo-optical coefficients in Sec. III B. A critical-point line-shape analysis is performed on the dielectric function in the vicinity of the E_1 and $E_1+\Delta_1$ transitions in Sec. III C, and in Sec. III D, strain deformation potentials are derived from the critical-point energies. The consistency of the deformation potentials with the stress dependence of the critical-point strengths and with the piezo-optical coefficients is checked in Secs. III E and III F, respectively. A tight-binding model is used to calculate piezo-optical coefficients and the deformation potentials for the E_1, $E_1+\Delta_1$ critical points; the results are compared with experimental data in Sec. IV.

II. EXPERIMENT

The experiments were performed on semi-insulating InP crystals (Fe-doped with 1.4×10^{18} atoms/cm^3). The samples were cut in $18\times2.8\times1.8$ mm^3 pieces, with the longest side along the [001] and [111] directions. The samples were aligned using Laue x-ray diffraction to an accuracy of $\pm0.2°$ and subsequently mechanically polished. A stress **X** was applied along the [001] axis (configuration $\mathbf{X}\|[001]$) or the [111] axis (configuration $\mathbf{X}\|[111]$), by using a stress apparatus,[35] which uses a hydraulic force transmission to apply compressive uniaxial stress. The stress apparatus allows accurate alignment of samples under stress, which is a necessity in ellipsometry. The samples were glued using epoxy resin in special cups, which fitted into the stress apparatus, and to which the force was applied. Before gluing, the samples were degreased in acetone and etched in a 50 °C solution of three parts H_2SO_4 (80%) and one part H_2O_2 (30%) for 1 min in order to remove native oxides. During the hardening of the glue, which typically took 6 h, a new oxide grew on the samples. By measuring the oxide thickness as a function of time, by spectroscopic ellipsometry (see below), we found that it reached a constant value of $\sim$20 Å after 3–5 h. The oxide thickness remained thus constant during the measurements of the stress-induced optical properties.

Ellipsometric measurements of the dielectric function were made for stresses from 0 to 0.7 GPa, in steps of 0.1 GPa; at higher stresses the samples broke. Taking into account the error in the measured sample cross sections ($\sim$1%) and in the applied forces (1–2 %), we estimate the stress values to be accurate to within 3%.

The ellipsometer,[36] of rotating analyzer type, had a Xe lamp as a light source and a double monochromator with gratings with 1200 lines/mm. Mirror optics was used. The polarizer and analyzer were prisms of Rochon type and the detector was a photomultiplier tube. The spectral range of our measurements was 1.6–5.5 eV ($\sim$825$-$225 nm) and the data were taken with an interval of 0.05 eV in the entire range, and of 0.005 eV in the 2.9–3.4 eV range, i.e., around the E_1-$E_1+\Delta_1$ transitions. The relative resolution was $\Delta E/E=6\times10^{-3}$. The angle of incidence was 67.5° and the incident light was linearly polarized with an angle of 30° with respect to the plane of incidence. The light was collimated by irises and the beam diameter was 4 mm. Conventional calibration procedures[37] were used prior to each measurement. An ellipsometric measurement gives the complex reflectance ratio between s- and p-polarized light. We used a three-phase model, see below, and standard formalism assuming sharp interfaces for the reflection process, to convert the measured complex reflectance ratios to complex dielectric functions.[38] All measurements were taken in air at room temperature.

TABLE I. Relations between change in dielectric function $\Delta\varepsilon$, stress X, and piezo-optical coefficients P_{ij}, for different uniaxial stresses **X**, crystallographic directions, faces, and electric fields **E**, used in the experiments.

$\mathbf{X}\|$	Face	$\mathbf{E}\|$	$\Delta\varepsilon$
[001]	(100)	[001]	$P_{11}X$
[001]	(100)	[010]	$P_{12}X$
[111]	$(\bar{2}11)$	[111]	$\frac{1}{3}(P_{11}+2P_{12}+2P_{44})X$
[111]	$(\bar{2}11)$	$[0\bar{1}1]$	$\frac{1}{3}(P_{11}+2P_{12}-P_{44})X$

For moderately anisotropic samples with large values of the dielectric functions, such as for InP under uniaxial stress, the dielectric function obtained from an ellipsometric measurement corresponds to a good approximation to the component of the dielectric tensor parallel to the intersection of the plane of incidence with the sample surface.[39] This feature was used to directly obtain the component of the dielectric tensor parallel $\varepsilon^{\|}$ and perpendicular $\varepsilon^{\perp}$ to the stress.

The piezo-optical coefficients were determined from the change in the measured dielectric functions with stress. The stress configurations, faces, and polarizations used in the experiments, and their relations to the piezo-optical components are summarized in Table I. Hence, P_{11} was determined from $\varepsilon^{\|}$ data under $\mathbf{X}\|[001]$ and P_{12} from the $\varepsilon^{\perp}$ data under $\mathbf{X}\|[001]$. Finally, P_{44} was determined from the difference between $\varepsilon^{\|}$ and $\varepsilon^{\perp}$ measured with $\mathbf{X}\|[111]$. We define compressive stress as negative, i.e., $X<0$ in our experiments. Notice that our definition of P_{44} differs from that used by Etchegoin and co-workers,[15–17] while those of P_{11} and P_{12} are the same (our definition of P_{44} is a factor 2 smaller than that of Etchegoin and co-workers). These definitions are used in the equations that relate the piezo-optical coefficients to the deformation potentials,[3] to be used below; therefore such factors are important. Our definition is consistent with that used by Nye[8] and Grechushnikov,[9] while that of Etchegoin and co-workers[15–17] was not in the case of P_{44}.

Ellipsometric measurements, especially in the ultraviolet, are sensitive to the presence of surface overlayers.[40,41] Hence, the measured dielectric functions were corrected with a three-phase model[38] for the presence of oxide overlayers. The oxide thicknesses of the unstressed samples were determined ellipsometrically by using the dielectric function of bulk InP (Ref. 42) and its oxide.[43] Thus, the oxide thickness was the only fitting parameter; it was found to be typically 20 Å. The fitted oxide thickness and the literature data for the oxide were then used to correct the dielectric function at all stresses. The crucial assumption here is that the dielectric function of the oxide does not change significantly with

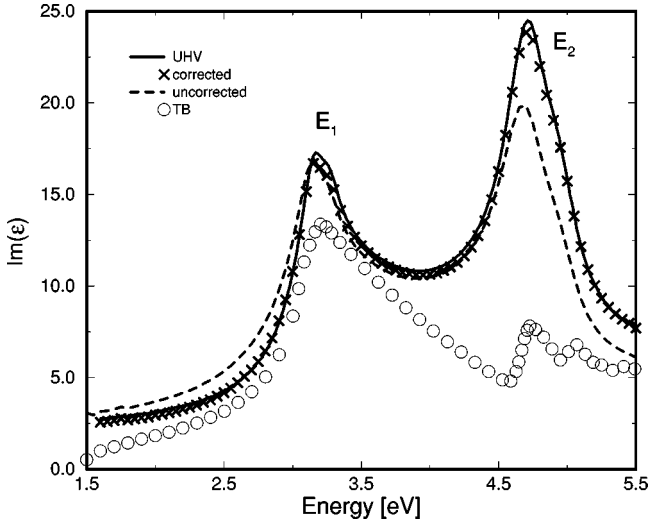

FIG. 1. The imaginary part of the dielectric function Im(ε) vs photon energy of unstressed InP at room temperature, as measured by rotating analyzer ellipsometry: data corrected for an oxide overlayer are shown as well as uncorrected data. Also shown are data obtained from InP cleaved and measured in ultrahigh vacuum (UHV) (solid line, from Ref. 42), and the result of a semiempirical tight-binding (TB) calculation. Note that the latter leads to a rather weak E_2 structure, resulting from too small a basis set.

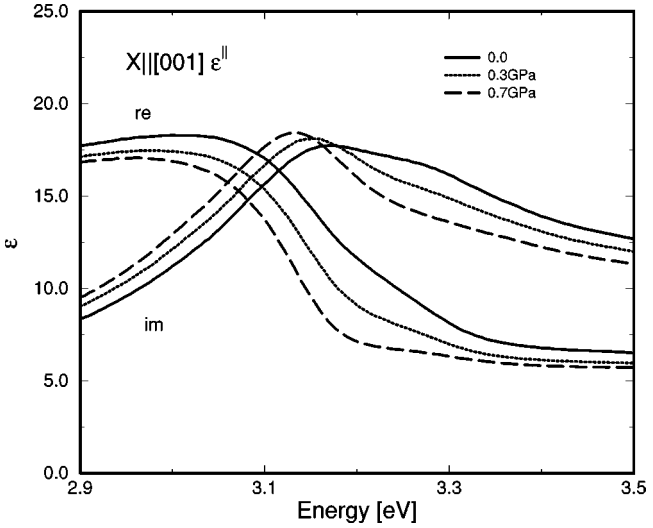

FIG. 2. Real, Re, and imaginary, Im, parts of the dielectric function ε around the E_1 and $E_1+\Delta_1$ transitions of InP vs photon energy, at different stresses, for stress $\mathbf{X}\|[001]$. Only the component parallel to the stress $\varepsilon^{\|}$ is depicted.

stress. We believe that this assumption is justified, since there are no critical points in the oxide dielectric function in our experimental energy range.[43]

III. RESULTS

A. Dielectric function

In Fig. 1, the imaginary part of the pseudodielectric function of InP is shown without correcting for the oxide overlayer. As can be seen in this figure, the difference between these results and those for InP cleaved and measured in ultrahigh vacuum[42] is significant, particularly above 4.5 eV, where the oxide is absorbing. However, the dielectric function corrected for an oxide overlayer reproduces the ultrahigh vacuum data reasonably well. Hence, our data after correcting for the oxide overlayer with the three-phase model can be reliably used for the determination of the piezo-optical constants. Our dielectric functions are also in good agreement with other ellipsometric data reported in the literature for InP.[40,41]

The changes in the dielectric function with stress are largest in the vicinity of critical points. In Fig. 2, an example of the change in $\varepsilon^{\|}$ with stress, $\mathbf{X}\|[001]$, for energies around the $E_1-E_1+\Delta_1$ transition, is given. The change in dielectric function with stress is clearly seen. The imaginary part reveals that for this configuration, the strength of the E_1 transition increases with stress, while that of the $E_1+\Delta_1$ transition decreases.

B. Piezo-optical coefficients

The piezo-optical coefficients were determined from the stress-induced changes of the dielectric function, as summarized in Table I. The piezo-optical coefficients P_{11} and P_{12} were determined from $\mathbf{X}\|[001]$ measurements. P_{44} was determined from the difference between $\varepsilon^{\|}$ and $\varepsilon^{\perp}$ measured with $\mathbf{X}\|[111]$, see Table I. Data up to 0.4 GPa were used. At higher stresses nonlinearities occur especially close to the critical points. Nonlinearities have also been observed for Ge (Ref. 15) and GaAs.[16] The piezo-optical coefficients obtained are shown in Fig. 3.

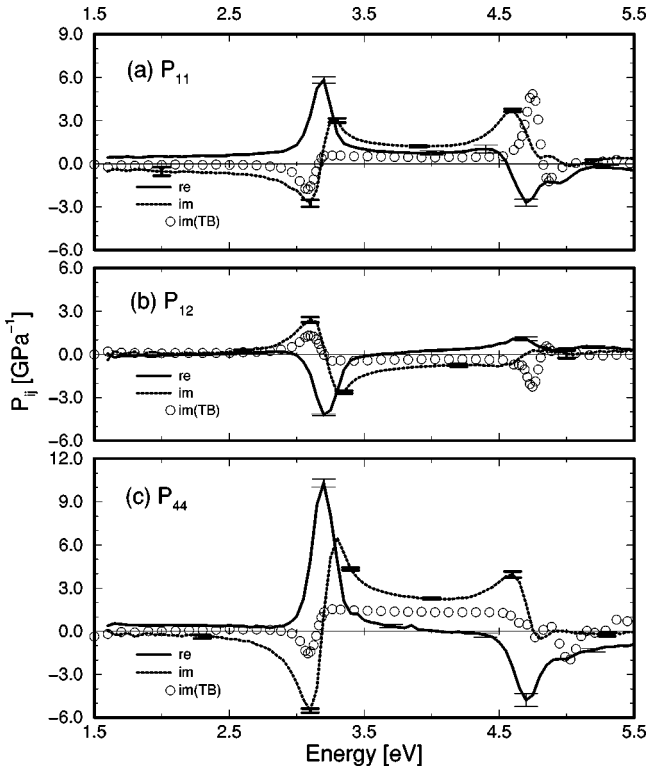

FIG. 3. Piezo-optical coefficients P_{11} (a), P_{12} (b), and P_{44} (c), (Re and Im parts) vs photon energy, for InP, at room temperature, as obtained from rotating analyzer ellipsometry. Also shown are imaginary parts of the piezo-optical coefficients as obtained from a semiempirical tight-binding (TB) calculation.

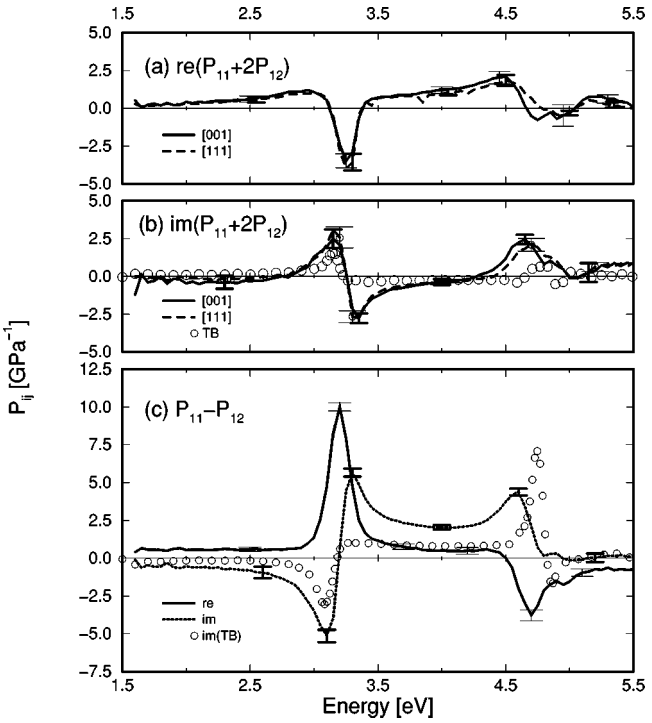

FIG. 4. (a) Real and (b) imaginary parts of the function $P_{11}+2P_{12}$ of InP, vs photon energy, as determined independently from experiments with stress $\mathbf{X}\|[001]$ and $\mathbf{X}\|[111]$. $P_{11}+2P_{12}$ corresponds to Γ_1 symmetry strain, such as the hydrostatic component. (c) The quantity $P_{11}-P_{12}$ (Re and Im parts) of InP, vs photon energy, which correspond to strain with Γ_{12} symmetry. The imaginary parts of $P_{11}+2P_{12}$ and $P_{11}-P_{12}$, calculated by using a semiempirical tight-binding model (TB) are also displayed in (b) and (c), respectively.

The error bars in Fig. 3 correspond to the variance of a least square fit of the dielectric function vs stress to a straight line. Since the piezo-optical coefficients are obtained from the change in the dielectric function with stress, any stress-independent systematic errors should largely cancel out. In this respect it should be mentioned that the oxide layer correction does affect the piezo-optical coefficients much less than the dielectric function itself. In fact, we obtained almost identical results for the piezo-optical coefficients determined from dielectric functions uncorrected for oxide overlayers.

We made two consistency tests of our piezo-optical coefficients: Kramers-Kronig (KK) consistency and self-consistency. Being linear and causal response functions, the real and imaginary parts of the piezo-optical coefficients are KK conjugate.[15] KK consistency is therefore necessary, but not sufficient, for the correct piezo-optical coefficients. Our InP data show KK consistency that is as good as those found for Ge,[15] GaAs,[16] and Si.[17]

The measurement of four independent quantities for the determination of three piezo-optical coefficients enables a self-consistency check to be made. The quantity $P_{11}+2P_{12}$ can be determined independently from both [001] and [111] data, cf. Table I. In Fig. 4, it can be seen that the data measured for these two stress directions are consistent within the estimated experimental errors. The good agreement supports the corrections of the experimental data. A measurement of the optical properties under hydrostatic pressure gives $P_{11}+2P_{12}$, but it is not easy to perform ellipsometric measurements on samples in a hydrostatic pressure cell. Judging from the self- and KK consistency of our data, we believe that they are correct.

In Fig. 4(c), the measured $P_{11}-P_{12}$ is shown. $P_{11}-P_{12}$ corresponds to the effect of the Γ_{12} irreducible strain component and can be obtained from the stress-induced birefringence with the stress along the [001] axis. With the stress along the [111] axis, the stress-induced birefringence gives P_{44}. Note that the line shapes of the two spectra, $P_{11}-P_{12}$ and P_{44}, are almost identical. As will be shown below, it follows from the small value of Δ_1 and does not apply to cases in which Δ_1 is larger, e.g., Ge (Ref. 15) and GaAs.[16]

C. Critical-point line-shape analysis

The measurement of stress-induced changes in the dielectric function can be further used to determine the shifts in the critical point energies. These shifts can be described by deformation potentials, which represent the change in energy eigenvalues induced by a unit change in the strain. We determine the deformation potentials for the E_1 and $E_1+\Delta_1$ transitions from the change in energies and strengths with stress. In order to determine the critical-point energies and strengths we use a standard analytical line shape for a two-dimensional critical point, such as E_1 and $E_1+\Delta_1$. We use for the E_1 transitions[44]

$$\varepsilon(E)=-A\frac{E_1^2}{E^2}\ln\left(1-\frac{E-i\Gamma_A}{E_1}\right)\exp(i\phi) \tag{3.1}$$

and for the $E_1+\Delta_1$ transitions[44]

$$\varepsilon(E)=-B\frac{(E_1+\Delta_1)^2}{E^2}\ln\left(1-\frac{E-i\Gamma_B}{E_1+\Delta_1}\right)\exp(i\phi). \tag{3.2}$$

In the actual fits we did not simply use Eqs. (3.1) and (3.2) but instead $\varepsilon(E)=[\varepsilon(E)+\varepsilon^*(-E)]/2$, which has the advantage of fulfilling the KK relations. The energies E_1 and $E_1+\Delta_1$, the strengths A and B, the lifetime broadenings Γ_A and Γ_B, and the phase ϕ were determined by fitting the second derivatives with respect to energy of Eqs. (3.1) and (3.2) to those of the experimental data. The phase ϕ was set to be identical in Eqs. (3.1) and (3.2). The real and imaginary parts were fitted simultaneously. The errors in the fitted parameters were taken as the 95% confidence interval.

In Fig. 5, the second derivatives of the imaginary parts of the dielectric functions $\varepsilon^{\|}$ and $\varepsilon^{\perp}$ are shown for three stresses, in the $\mathbf{X}\|[001]$ configuration, together with fittings to Eqs. (3.1) and (3.2). For clarity reasons, in Fig. 5 only the imaginary part is displayed. The fitted curves clearly demonstrate that the critical-point energies and strengths change with applied stress. A comparison between Fig. 5(a) and Fig. 2 illustrates the well-known fact that these effects are more pronounced in the second derivative of the dielectric function than in the dielectric function itself. Note that for $\mathbf{X}\|[001]$ and $\varepsilon^{\|}$, the strength of the E_1 transitions increases and the $E_1+\Delta_1$ transition decreases with stress. For $\varepsilon^{\perp}$ the opposite is found.

The line-shape parameters determined by us for unstressed InP at room temperature are compared in Table II with other values found in the literature.[40,45–47] Our param-

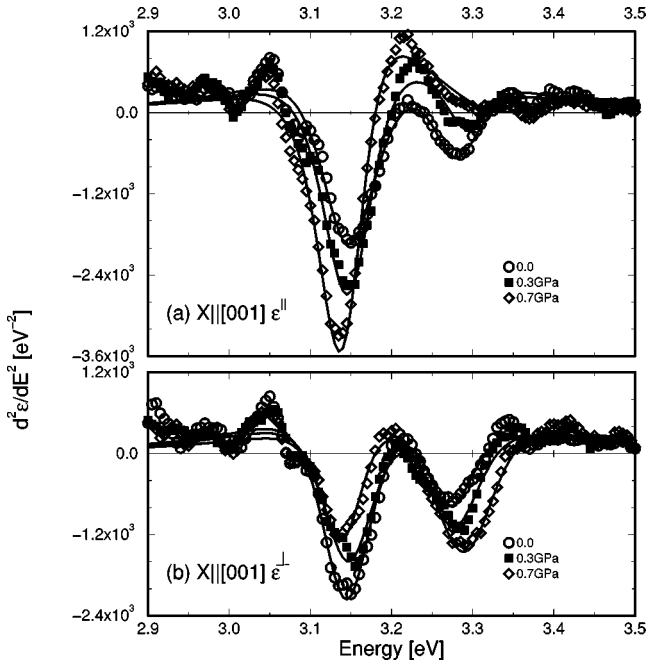

FIG. 5. Second derivatives of the imaginary part of the dielectric function of InP around the E_1 and $E_1+\Delta_1$ critical points, for stress $\mathbf{X}\|[001]$. Second derivatives of the components parallel $\boldsymbol{\epsilon}^{\|}$ and perpendicular $\boldsymbol{\epsilon}^{\perp}$ to the [001] axis are shown for three values of the stress. The solid lines were calculated to fit the experimental data, by using an analytical expression for a two-dimensional critical point.

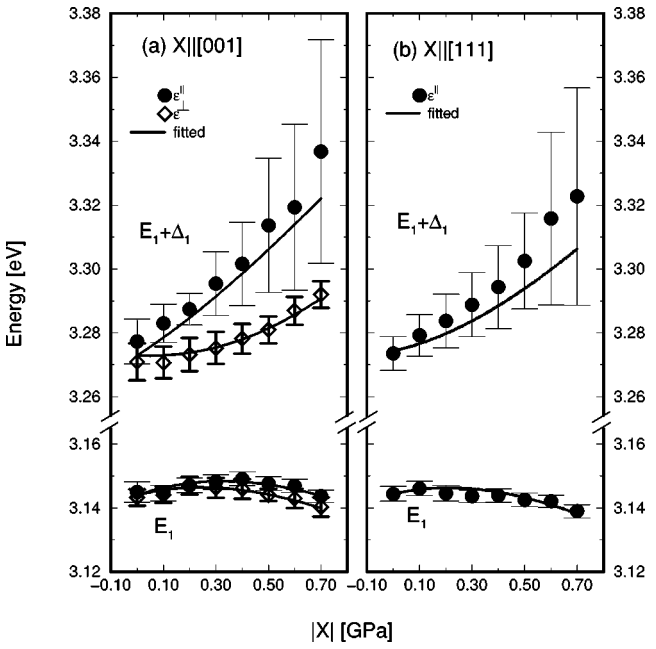

FIG. 6. Energy eigenvalues E_1 and $E_1+\Delta_1$ for InP, vs stress $\mathbf{X}$ for the incident electric field parallel $\varepsilon^{\|}$ and perpendicular $\varepsilon^{\perp}$ to the stress, for (a) $\mathbf{X}\|[001]$, and (b) for $\mathbf{X}\|[111]$. Also shown are fitted curves, from which (a) the deformation potentials D_1^1 and D_3^3 and the spin-exchange parameters δ_{J1} and δ_{J2}, and (b) the deformation potentials D_1^5 and D_3^5 were determined.

eters are in good agreement with the earlier determinations. Note that the error bars are rather different for the different parameters. The energies E_1 and $E_1+\Delta_1$ are the most accurate ones, while the errors in the broadenings Γ_A and Γ_B and particularly in the relative strengths B/A are noticeably larger.

D. Critical-point energies and deformation potentials

The energies are the best determined line-shape parameters (see Table II) and we therefore use them to determine the deformation potentials of the E_1 and $E_1+\Delta_1$ transitions.

In Fig. 6(a), the energies for the E_1 and $E_1+\Delta_1$ transitions are plotted as a function of stress for $\mathbf{X}\|[001]$, and in Fig. 6(b) for $\mathbf{X}\|[111]$. The errors in the energies are larger for the $E_1+\Delta_1$ than for the E_1 transition, due to the lower strength of the former (see Fig. 5 and Table II). At high stresses, the errors in the determination of $E_1+\Delta_1$ become large in Fig. 6(a), for $\mathbf{X}\|[001]$ and $\varepsilon^{\|}$, since the strength of the measured structures decreases with stress (see Fig. 5). This also explains the larger errors in $E_1+\Delta_1$ displayed in Fig. 6(b), especially at high stresses.

The L-point energy eigenvalues for $\mathbf{X}\|[001]$ are given by[14,48–51]

$$E(X)=E_1+\frac{\Delta_1}{2}+\delta_H\pm\left[\left(\frac{\Delta_1}{2}\right)^2+(\delta_J\pm\delta_S)^2\right]^{1/2}, \quad (3.3)$$

where $\delta_H=(D_1^1/\sqrt{3})(S_{11}+2S_{12})X$ and $\delta_S=\sqrt{2/3}D_3^3(S_{11}-S_{12})X$. The first set of $\pm$ signs gives the stress dependence of E_1 $(-)$ and $E_1+\Delta_1$ $(+)$, respectively. The second gives the difference in energy eigenvalues for $\varepsilon^{\|}$ $(-)$ and $\varepsilon^{\perp}$ $(+)$. D_1^1 represents the deformation potential for hydrostatic strain, D_3^3 is the intraband effect of a [001] shear strain on the valence band, and δ_J is a spin-exchange term, which causes splitting of E_1 and $E_1+\Delta_1$ for $\varepsilon^{\|}$ and $\varepsilon^{\perp}$. Experimentally it is often found that δ_J is different for the E_1 and $E_1+\Delta_1$ transitions. We denote the spin-exchange term for the

TABLE II. Line-shape parameters of InP at room temperature as determined from spectroscopic ellipsometry.

E_1 (eV)	$E_1+\Delta_1$ (eV)	Γ_A (meV)	Γ_B (meV)	B/A	ϕ (deg)	Ref.
3.158 ±0.004	3.291±0.004	64±2	63±5	0.5±0.15	57±5	45 [a]
3.1484±0.0024	3.2896±0.0056	70.4±3.4	64.2±8	0.36	35.6±4.3, 28.5±10.8	46 [b]
3.157	3.293	83.5	83.5	0.31	106±4	47 [b]
3.149	3.275					40 [b]
3.144 ±0.003	3.274±0.006	63.6±3.5	57.2±5.6	0.37±0.06	83.5±4	This work [b]

[a]Three-dimensional critical point, third-order derivative analyzed.

[b]Two-dimensional critical point, second-order derivative analyzed.

TABLE III. Deformation potentials and spin-exchange parameters for the E_1 and $E_1+\Delta_1$ transitions in InP. Rows 1 and 2 are experimental values and rows 3–11 are theoretical.

	D_1^1 (eV)	D_1^5 (eV)	D_3^3 (eV)	D_3^5 (eV)	δ_{J1} (meV)	δ_{J2} (meV)	Ref.
1	-9.1 ± 1.4 [a,d,f]	20.4 ± 6.4 [b,d,f]	-4.1 ± 0.3 [a,d,f]	-12.9 ± 2.5 [b,d,f]	3 ± 3 [a,d,f]	-25 ± 13 [a,d,f]	This work
2	-9.0 [c,e,f]						22
3	-2.06 [a,k]	11.08 [b,k]	-3.00 [a,k]	-6.59 [b,k]			This work
4		20.04 [b,k,m]					This work
5	-3.93 [a,l]	12.85 [b,l]	-3.05 [a,l]	-7.10 [b,l]			This work
6		19.43 [b,l,m]					This work
7	-4.76 [g]						32
8	-4.77 ± 0.13 [h]						29
9	-6.56 [h]						31
10	-4.64 [i]						30
11	-8.0 [j]						27

[a]Uniaxial stress, $\mathbf{X}\|[001]$.
[b]Uniaxial stress, $\mathbf{X}\|[111]$.
[c]Hydrostatic stress.
[d]Ellipsometry.
[e]Electroreflectance.
[f]Room temperature.
[g]LDA.
[h]LMTO.
[i]First-principles pseudopotential (relativistic).
[j]Empirical pseudopotential.
[k]Tight binding, ε.
[l]Tight binding, L point.
[m]$D_1^1=-9.1$ eV used.

E_1 transition δ_{J1} and for the $E_1+\Delta_1$ transition δ_{J2}. S_{11} and S_{12} are elastic compliance constants.

The deformation potentials D_1^1 and D_3^3 and the spin-exchange terms δ_{J1} and δ_{J2} were determined by fitting Eq. (3.3) to the experimentally found energies. Since D_3^3 appears as a quadratic term in Eq. (3.3), its sign was determined from the stress-induced change of the critical-point strengths, as described below. The values $S_{11}=16.4$ TPa^{-1} and $S_{12}=-5.9$ TPa^{-1} were taken from the literature.[52] In the fitting procedure, the points were given weights proportional to the inverse of the square of their errors. The fitted curves are shown by the solid lines in Fig. 6(a) and the determined deformation potentials are summarized in Table III. Our value for D_1^1 is in good agreement with that of Bendoryus and Shileika.[22]

For $\mathbf{X}\|[111]$, the energy eigenvalues are split into a singlet (S), corresponding to the [111] direction in $\mathbf{k}$ space, and a triplet (T), corresponding to $[1\bar{1}\bar{1}]$, $[\bar{1}1\bar{1}]$, and $[\bar{1}\bar{1}1]$. The stress dependence of the singlet and triplet is given by[14,49,51]

$$E^S(X)=E_1+\frac{\Delta_1}{2}\pm\frac{\Delta_1}{2}-\delta_H+\frac{\delta_{S'}}{2}, \tag{3.4}$$

$$E^T(X)=E_1+\frac{\Delta_1}{2}-\delta_H-\left(\frac{\delta_{S'}}{6}\right)\pm\left[\left(\frac{\Delta_1}{2}\right)^2+\frac{4}{9}\delta_{S''}^2\right]^{1/2}, \tag{3.5}$$

where $\delta_{S'}=(D_1^5/\sqrt{3})S_{44}X$ and $\delta_{S''}=(D_3^5/\sqrt{6})S_{44}X$. The energy eigenvalues of the E_1 and $E_1+\Delta_1$ transitions are given by the $(-)$ and $(+)$ signs, respectively. Here, D_1^5 represents the intervalley effect of a [111] shear strain on the E_1 and $E_1+\Delta_1$ critical-point gaps, while D_3^5 describes the intravalley effect of the corresponding valence bands. $S_{44}=21.7$ TPa^{-1} is an elastic compliance constant.[52]

For $\mathbf{X}\|[111]$, $\varepsilon^{\|}$ has only a contribution from the triplet, while $\varepsilon^{\perp}$ has contributions from both the singlet and the triplet. We therefore determined D_1^5 and D_3^5 by fitting Eq. (3.5) to the experimental data for $\varepsilon^{\|}$. The sign of D_3^5, which appears as a quadratic term in Eq. (3.5), was determined from the stress-induced changes of the critical-point strengths, as described below. Again, the points were given weights proportional to the inverse of the square of their errors. We used the value of D_1^1 determined from the $\mathbf{X}\|[001]$ data. The fitted curves are shown in Fig. 6(b) while the deformation potentials are given in Table III.

The estimated errors are relatively large for D_1^1 and D_1^5, which appear as linear terms in Eqs. (3.3) and (3.5). Since D_1^1, as determined from $\mathbf{X}\|[001]$ results, was used when analyzing the $\mathbf{X}\|[111]$ measurements, the error in D_1^5 is also affected by the error in D_1^1. Furthermore, D_3^3 and D_3^5 appear as quadratic terms in Eqs. (3.3) and (3.5), therefore the relative errors are smaller. Finally, δ_{J1} and δ_{J2} have large relative errors. In Eq. (3.3) they have been assumed to be identical. Our experimental values of δ_{J1} and δ_{J2} for InP are, however, different. Also for Ge[15] and GaAs,[16] δ_{J1} and δ_{J2} have been found not to have the same value, as would be expected on the basis of exchange interaction between the E_1 and $E_1+\Delta_1$ states. Our fitted values of δ_{J1} and δ_{J1} seem to have even opposite signs, although δ_{J1} is nearly zero. This seems to be the case also for GaAs in Ref. 53. We do not at this time have any explanation for this feature.

For Ge and GaAs, $\delta_J\ll\delta_S\ll\Delta_1/2$ and $\delta_{S''}\ll\Delta_1/2$. Therefore, Eqs. (3.3) and (3.5) can be linearized. These approximations are not valid for InP because of the small value of

Δ_1. Hence, the deformation potentials have to be determined by simultaneously fitting both E_1 and $E_1+\Delta_1$ in Eqs. (3.3) and (3.5), respectively, to the experimentally determined energies.

E. Critical-point strengths and deformation potentials

Not only the change in critical-point energies, but also the change in their strengths with stress, can be used to determine deformation potentials. The relative errors in the strengths are, however, normally larger than those of the energies (see Table II). We therefore defer from determining the deformation potentials from strength changes and, instead, use the data only for the consistency checks. In Eqs. (3.3) and (3.5), D_3^3 and D_3^5 appear as quadratic terms. Hence, only their magnitudes can be determined. However, the change in the strength of the critical points with stress can be used to determine the signs of D_3^3 and D_3^5. For $\mathbf{X}\|[001]$ the strengths are[14,49,51]

$$I^{\|}_{E_1}(X)=I_{E_1}(0)(1+\alpha_1), \tag{3.6}$$

$$I^{\|}_{E_1+\Delta_1}(X)=I_{E_1+\Delta_1}(0)(1-\alpha_1, \tag{3.7}$$

$$I^{\perp}_{E_1}(X)=I_{E_1}(0)(1-\tfrac{1}{2}\alpha_1), \tag{3.8}$$

and

$$I^{\perp}_{E_1+\Delta_1}=I_{E_1+\Delta_1}(0)(1+\tfrac{1}{2}\alpha_1), \tag{3.9}$$

where $\alpha_1=\sqrt{8/3}D_3^3(S_{11}-S_{12})X/\Delta_1$. Equations (3.6)–(3.9) are valid for $(\alpha_1)^2\ll 1$.

For $\mathbf{X}\|[111]$ the corresponding strengths are[14,49,51]

$$I^{\|}_{E_1}(X)=I_{E_1}(0)(1+\tfrac{4}{3}\alpha_2), \tag{3.10}$$

$$I^{\|}_{E_1+\Delta_1}(X)=I_{E_1+\Delta_1}(0)(1-\tfrac{4}{3}\alpha_2), \tag{3.11}$$

$$I^{\perp}_{E_1}(X)=I_{E_1}(0)(1-\tfrac{2}{3}\alpha_2), \tag{3.12}$$

and

$$I^{\perp}_{E_1+\Delta_1}=I_{E_1+\Delta_1}(0)(1+\tfrac{2}{3}\alpha_2), \tag{3.13}$$

where $\alpha_2=D_3^5/\sqrt{6}S_{44}X/\Delta_1$. Equations (3.10)–(3.13) are valid for $(\alpha_2)^2\ll 1$.

In Figs. 7(a) and 7(b) the normalized strengths for the E_1 and $E_1+\Delta_1$ transitions are shown for $\mathbf{X}\|[001]$. Also displayed are calculated relative strengths, from Eqs. (3.6)–(3.9) using D_3^3 as determined above (see Table III). Figures 7(c) and 7(d) show the relative strengths for $\mathbf{X}\|[111]$. The D_3^5 given in Table III was used in Eqs. (3.10)–(3.13). The signs of D_3^3 and D_3^5 in Table III gives the correct increases and decreases of the critical point strengths with stress calculated from Eqs. (3.6)–(3.13). We therefore conclude that the signs of D_3^3 and D_3^5 given in Table III are correct.

The straight lines in Figs. 7(a)–7(d) were obtained from Eqs. (3.6)–(3.9) and (3.10)–(3.13), and should be valid for $(\alpha_1)^2\ll 1$ and $(\alpha_2)^2\ll 1$, respectively. If we assume that Eqs. (3.6)–(3.13) are valid for $\alpha_{1,2}\leqslant 0.3$ $[(\alpha_{1,2})^2\leqslant 0.1]$, the corresponding ranges of stresses should be $|\mathbf{X}|\leqslant 0.35$ GPa for both $\mathbf{X}\|[001]$ and $\mathbf{X}\|[111]$. If we compare the straight lines in Figs. 7(a)–7(d) with the experimental values, this region of validity appears to be correct. Thus not only the signs of D_3^3 and D_3^5 in Table III, but also the numerical values are in agreement with the stress-induced changes in critical-point strengths.

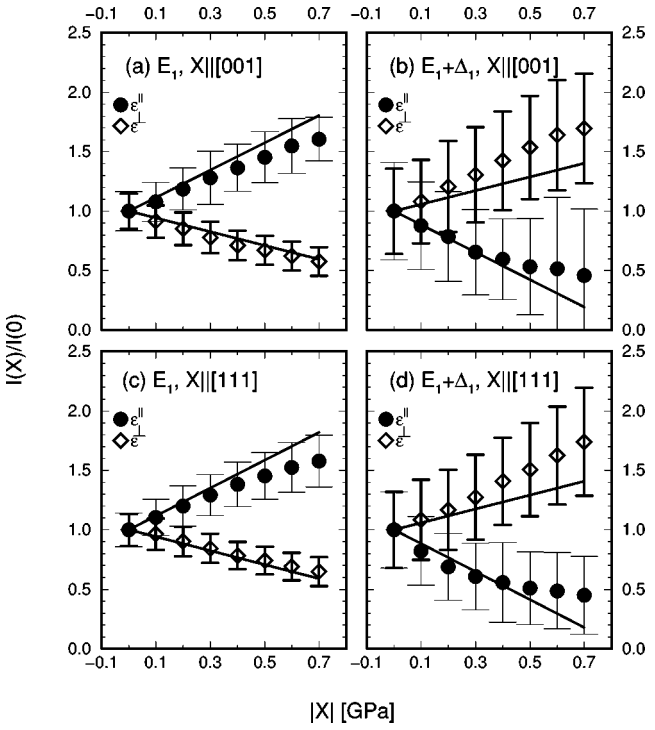

FIG. 7. Relative critical-point strengths for InP vs stress $\mathbf{X}\|[001]$, for the (a) E_1 and (b) $E_1+\Delta_1$ transitions, and for stress $\mathbf{X}\|[111]$ (c) and (d). The sign of D_3^3 was determined from (a) and (b) with $D_3^3=-4.1$ eV. The sign of D_3^5 was determined from (c) and (d) with $D_3^5=-12.9$ eV.

F. Piezo-optical coefficients and deformation potentials

Both the piezo-optical coefficients and the deformation potentials are measures of the change in the electronic structure with stress and model expressions can be found describing the relation between the piezo-optical coefficients and the deformation potentials.[3] We will now use these relations to check the consistency between piezo-optical coefficients and deformation potentials determined in this work. In principle, the deformation potentials could be determined from the piezo-optical coefficients.[54] For InP, as we shall see, this appears not to be a good method due to the large difference in critical-point strength of the E_1 and $E_1+\Delta_1$ transitions (see Table II). It provides, however, an additional consistency check of the data.

The hydrostatic deformation potential, D_1^1, is related to $P_{11}+2P_{12}$ by[3]

$$P_{11}+2P_{12}=\frac{D_1^1}{\sqrt{3}}\frac{d\varepsilon}{dE_1}3(S_{11}+2S_{12}), \tag{3.14}$$

where, $3(S_{11}+2S_{12})=1/B$, B being the bulk modulus, and $d\varepsilon/dE_1$ can be expressed as[3]

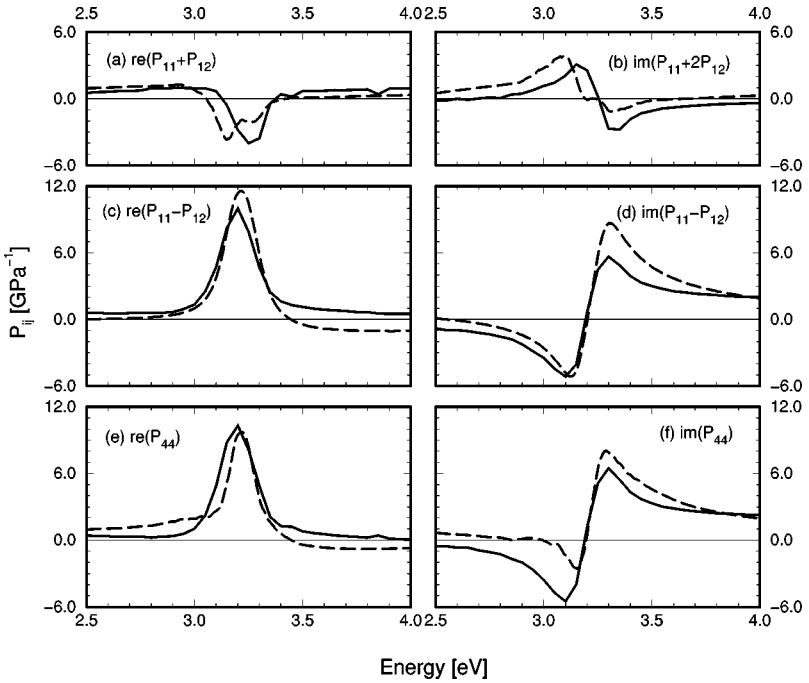

FIG. 8. Re and Im parts of the functions $P_{11}+2P_{12}$ [(a) and (b)], $P_{11}-P_{12}$ [(c) and (d)] and P_{44} [(e) and (f)], in the vicinity of the E_1 and $E_1+\Delta_1$ transitions of InP, as measured by ellipsometry (solid lines) and as calculated from Eqs. (3.14)–(3.17) (dashed lines), using deformation potentials determined from the change in E_1 and $E_1+\Delta_1$ with stress (Table III).

$$\frac{d\varepsilon}{dE_1}=-\frac{E}{E_1}\frac{d\varepsilon}{dE}-\frac{2}{E}\varepsilon. \tag{3.15}$$

The quantity $P_{11}-P_{12}$, which describes the effects of strains of Γ_{12} symmetry, is related to D_3^3, the deformation potential describing a [001] shear strain (also of Γ_{12} symmetry):[3]

$$P_{11}-P_{12}=\sqrt{6}D_3^3\left(\frac{\varepsilon^{(E_1)}-\varepsilon^{(E_1+\Delta_1)}}{\Delta_1}\right)(S_{11}-S_{12}). \tag{3.16}$$

Here, $\varepsilon^{(E_1)}$ and $\varepsilon^{(E_1+\Delta_1)}$ are the contributions to the dielectric function from the E_1 and $E_1+\Delta_1$ transitions, respectively.

Finally, P_{44}, which corresponds to strains of Γ_{15} symmetry, can be written as a function of D_1^5 and D_3^5,[3]

$$P_{44}=\frac{1}{4\sqrt{3}}\left[-D_1^5\frac{d\varepsilon}{dE_1}+4\sqrt{2}D_3^5\left(\frac{\varepsilon^{(E_1)}-\varepsilon^{(E_1+\Delta_1)}}{\Delta_1}\right)\right]S_{44}. \tag{3.17}$$

We now take the deformations potentials obtained from the stress-induced changes of E_1 and $E_1+\Delta_1$, (Table III) and calculate the piezo-optical coefficients according to Eqs. (3.14)–(3.17). In Eq. (3.15) we use the experimental values for ε and $d\varepsilon/dE$. For $\varepsilon^{(E_1)}$ and $\varepsilon^{(E_1+\Delta_1)}$ we use Eqs. (3.1) and (3.2) with the parameters determined from the analysis of the second derivative of ε, see Table II. We found however, that equal strength for $\varepsilon^{(E_1)}$ and $\varepsilon^{(E_1+\Delta_1)}$ had to be used in order to reproduce the experimental line shapes.

In Figs. 8(a) and 8(b), $P_{11}+2P_{12}$, calculated from Eqs. (3.14) and (3.15), is shown. Both the real and imaginary parts are reproduced reasonably well.

In Figs. 8(c)–8(f), $P_{11}-P_{12}$ and P_{44}, calculated from Eqs. (3.16) and (3.17), are displayed. The line shapes of $P_{11}-P_{12}$ and P_{44} are very similar, since both are dominated by the D_3^5 term. The D_1^5 term in Eq. (3.17) gives a minor contribution to P_{44}.

As mentioned above, the line shapes of $P_{11}-P_{12}$, and also P_{44}, are well reproduced by Eqs. (3.16) and (3.17), only if the same strengths are used for the E_1 and $E_1+\Delta_1$ transitions. This is in sharp contrast to the experimentally determined ratio between the two strengths, $B/A=0.37$ (see Table II). Equations (3.14)–(3.17) were derived within a one-electron approximation, within which the strengths of the E_1 and $E_1+\Delta_1$ transitions should be almost the same. The experimentally found difference is probably due to excitonic effects (exchange interaction). A similar effect has been seen in the Raman polarizability of Ge,[55] where in the expression corresponding to Eq. (3.17), the line-shape parameters of $\varepsilon^{(E_1)}$ and $\varepsilon^{(E_1+\Delta_1)}$ as determined from ellipsometry, were used, except for the strengths that were taken to be those found with the one-electron approximation.

IV. TIGHT-BINDING CALCULATIONS

The previous analysis of the pressure-induced changes in the optical properties of InP was performed using a two-dimensional critical-point model that is valid only in the region of **k** along [111] in which valence and conduction bands are nearly parallel. In order to have a different, possibly more realistic description of the optical properties and the corresponding effects of stress, it is necessary to take into account stress effects over the entire Brillouin zone. Such an approach requires a microscopic calculation of the optical properties. In this section, we present a detailed theoretical analysis of pressure effects on the optical properties of InP using the empirical tight-binding method (ETBM). This method allows the determination of the dielectric constant, of the piezo-optical coefficient, and of the deformations potentials[28] of InP.

The ETBM calculations used a basis of sp^3s^* orbitals[56] with only nearest-neighbor interactions. The calculations include the spin-orbit coupling; this interaction expands the basis to a total of 10 orbitals per atom. The tight-binding on-site and overlap parameters were obtained by refining

TABLE IV. Tight-binding parameters (in eV) for InP. The notation for the parameters corresponds to that of Ref. 58. The indices 0 and 1 correspond to the P and In atoms, respectively. Δ_0 and Δ_1 are the spin-orbit parameters for P and In, respectively, obtained from Ref. 65.

E_{s_0}	E_{p_0}	E_{s_1}	E_{p_1}	V_{ss}	V_{xx}	V_{xy}	V_{s_0p}	V_{s_1p}	$E_{s_0^*}$	$V_{s_0^*p}$	$E_{s_1^*}$	$V_{s_1^*p}$	Δ_0	Δ_1
−8.681	0.7379	−0.8751	4.135	−4.81	1.773	4.253	2.51	5.582	8.264	3.462	7.067	4.483	6.70E-02	0.392

those published in Ref. 56 in order to correctly account for the spin-orbit interaction. In the refining procedure, the calculated critical-point energies were fitted to experimental values at high-symmetry points of the Brillouin zone, when available, or to empirical pseudopotential calculations.[57]

The calculations of the imaginary part of the dielectric function ε_2 requires the integration of all optical transition elements between valence and conduction states over the Brillouin zone. These elements were obtained directly from the tight-binding Hamiltonian following the procedure described in Ref. 58. In this way, no extra parameters are required for the determination of the optical properties in addition to those listed in Table IV. ε_2 was then determined by randomly sampling the Brillouin zone using a large number of k points (typically 10^7) in order to obtain good statistics. The real part, ε_1, can be found by a KK transformation of ε_2.

The calculated values of ε_2 for InP are displayed as circles in Fig. 1 and compared to the experimental values. Note that while the calculation reproduces well the position of the critical points, the strengths are normally underestimated. This discrepancy arises from the approximations used in the calculations: the ETBM uses a basis consisting of very few orbitals, it does take into account only nearest-neighbor interactions, and it completely neglects local field and excitonic effects. Also, the agreement is less satisfactory for the higher-energy E_0' and E_2 transitions. This is attributed to the fact that the parametrization in Table IV was optimized to describe the band structure near the fundamental and the E_1 gaps. Using an empirical pseudopotential method, Etchegoin and co-workers[15,16] found that the strengths of the E_1 and $E_1+\Delta_1$ transitions were lower than the experimental ones. Using a Lorentzian broadening these authors showed that the agreement around the E_0' transition of GaAs could be improved.

The quality of the calculated ε_2 data in Fig. 1 is good enough to attempt a calculation of the second derivative and the fitting of these calculations to expressions of the type of Eqs. (3.1) and (3.2). By doing so one obtains a ratio $B/A \sim 0.87$ between the ratios of the E_1 and $E_1+\Delta_1$ transitions. The deviation of the B/A ratio from unity can be attributed to the weak $\mathbf{k}\cdot\mathbf{p}$ coupling between the $\Lambda_4-\Lambda_5$ and the spin-split Λ_6 bands for $\Gamma<\mathbf{k}<L$.[59] This coupling decreases the transverse mass (i.e., perpendicular to the [111] direction) of the $\Lambda_4-\Lambda_5$ band and increases that of the Λ_6 band, thus changing the relative strength of the E_1 and $E_1+\Delta_1$ transitions. Note, however, that this effect should be relatively weak and cannot explain the large difference $B/A=0.37$ between the strengths observed in the experimental data. The results presented here give further evidence for the fact that that small B/A cannot be explained within the framework of the one-electron theory, as already discussed in Sec. III F.

The stress-induced changes in the electronic structures were calculated by taking into account the microscopic modifications of the atomic positions and of the tight-binding overlap parameters with the bond lengths and angles. For the latter, we used here the simple model proposed by Harrison,[60] where the intersite parameters between s and p orbitals scale with the inverse square of the bond length. For $\mathbf{X}\|[001]$, the atomic coordinates under pressure are completely described by the elastic constants of the medium. For $\mathbf{X}\|[111]$ the positions of the atoms in the unit cell are not completely described by the elastic constant but require knowledge of the internal displacement parameter ζ.[61] We used the value $\zeta=0.699$ estimated by Martin.[62]

The piezo-optical coefficients P_{11}, P_{12}, and P_{44} were determined from calculations for the components of the dielectric function in the directions parallel and perpendicular to the stress. The procedure used here is similar to that followed in the experiments (see Table I). The stresses used in the calculations were the same as those used in the experiments. The calculated values for the imaginary part of these coefficients are displayed as circles in Figs. 3 and 4. As for the dielectric function, the spectral lineshape is reasonably well reproduced by the calculations, specially near the E_1 transition. The strengths, however, are normally underestimated. Among the reasons for these discrepancies are the previously mentioned simplifications used in the calculations. Another reason lies in the underestimation of the deformations potentials, to be described in detail below. In a recent paper,[63] Theodorou and Tsegas used an empirical tight-binding model to calculate the piezo-optical properties of Ge. Their calculations also reproduce the spectral line shapes near the E_1 transition, but the strenghs are lower than what has been found experimentally.[15]

The deformation potentials for the E_1 and $E_1+\Delta_1$ transitions were determined using the tight-binding method following two different approaches. The first consisted in calculating the shift of the transition energies between the Γ and L points (i.e., 111 states) of the band structure, for different values and orientation of the stress. By analyzing these data using Eqs. (3.3) to (3.5), we obtained the deformation potentials shown in Fig. 9(a). The deformation potentials at the L point are also listed in row 5 of Table III. In Figs. 9(b) and 9(c), respectively, calculated energies of the E_1 transition between Γ and L are displayed as well as their corresponding matrix elements $\langle p\rangle^2$. The largest contribution to the optical properties is from transitions close to the L point, where the joint density of states is highest. Note that in this region the deformation potential, energies, and transition matrix elements are practically independent of k.

The second procedure for calculating the deformation potentials consisted in calculating the full dielectric constant for different stress values. The critical-point energy shifts were then determined by fitting the second derivative of the calculated data to expressions (3.1) and (3.2). This procedure, which is similar to the one used to analyze the experimental data, yields the deformation potentials in row 3 of

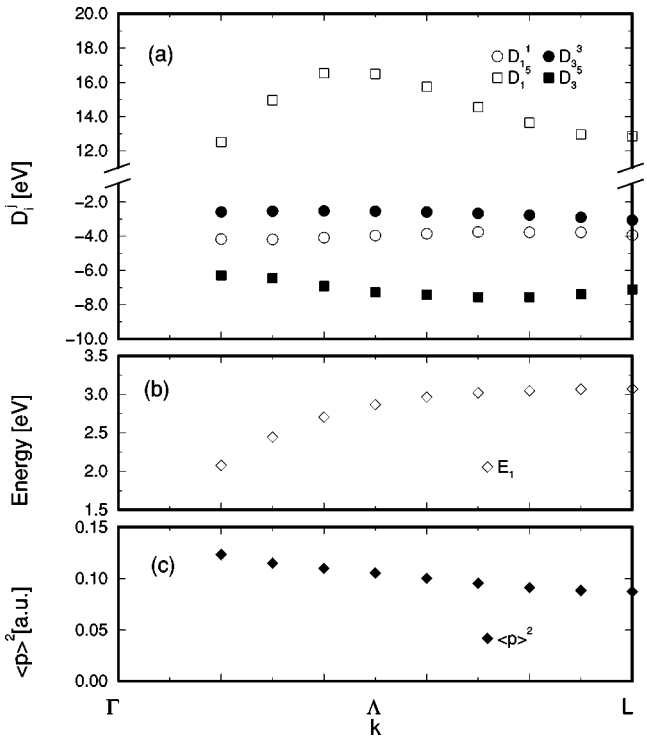

FIG. 9. (a) Deformation potentials, D_i^j, (b) transition energies E_1, and (c) matrix elements $\langle p \rangle^2$ (in atomic units) for the E_1 transition of InP, between Γ and L as obtained from a semiempirical tight-binding calculation.

Table III. As an advantage, the latter procedure takes automatically into account contributions over the full Brillouin zone, and does not require an averaging over contribution of different points.[64]

The calculations reproduce the sign of all experimentally measured deformation potentials (see Table III). Also, except for D_1^1, the two procedures described above yield essentially the same results for the deformation potentials. This result indicates that the main contribution to the deformation potentials comes from the region near the L point where the valence and conduction bands are almost parallel. The tight-binding calculations, however, underestimate the absolute values of the calculated deformation potentials. The underestimation becomes especially large for D_1^1 ($D_1^1 = -3.93$ eV in the 5th row of Table III in comparison with an experimental value of $D_1^1 = -9.1$ eV). A probable reason for the small values of the calculated deformation potentials lies in the functional form used to describe the dependence of the intersite tight-binding parameters with bond length.[60] It is important to note, however, that the discrepancies between theoretical and experimental values are not specific to the ETBM. In fact, even more advanced calculation methods yield D_1^1 values between -4 eV and -8 eV, as illustrated in rows 7–11 of Table III.

Except for D_1^1, values for the other deformation potentials of InP have not been calculated previously. The ETBM reproduces reasonably well the experimental value of D_3^3 and, to a lesser extent, of D_3^5 and D_1^5. The lower calculated values of D_1^5 can be traced back to the lower value of D_1^1. In fact, if the experimentally measured value of $D_1^1 = -9.1$ eV is used to analyze the tight-binding results, one obtains values very close to experimental results (see rows 4 and 6 of Table III).

V. CONCLUSIONS

We have measured the piezo-optical coefficients of InP in the 1.6–5.5 eV range using ellipsometric methods. Two prominent set of features are related to the E_1, $E_1+\Delta_1$ and the E_2 interband critical points. The E_1, $E_1+\Delta_1$ features have been fitted with analytic line-shape expressions. From those, numerical values for several deformation potentials have been extrapolated. These deformation potentials have been compared with the results of band-structure calculations. A full calculation of the piezo-optic spectra based on a tight-binding band structure has been shown to provide a reasonable representation of the measured spectra.

ACKNOWLEDGMENTS

We would like to thank H. Hirt, P. Hiessl, and M. Siemers for technical assistance and I. Silier for help with the sample preparation. L. F. Lastreis-Martínez is acknowledged for valuable comments on the manuscript. Thanks are also due to the Fonds der Chemischen Industrie for financial support.

[1] M. Cardona, in *Optical Properties and Band Structure of Germanium and Zincblende-Type Semiconductors*, edited by E. Burstein, Proceedings of the International School of Physics ''Enrico Fermi'' (Academic Press, New York, 1972), p. 514.

[2] D. E. Aspnes, in *Handbook on Semiconductors*, edited by T. S. Moss (North-Holland, Amsterdam, 1980), p. 109.

[3] M. Cardona, in *Light Scattering in Solids II*, edited by M. Cardona and G. Güntherodt (Springer-Verlag, Berlin, 1982), p. 19.

[4] B.J. Jusserand and M. Cardona, in *Light Scattering in Solids V, Superlattices and Other Microstructures*, edited by M. Cardona and G. Güntherodt (Springer, Berlin, 1989), p. 49.

[5] T. Pearsall, *Strained-Layer Superlattices: Physics of Semiconductors and Semimetals Vol. 32* (Academic Press, Orlando, FL, 1990).

[6] D. Toet, B. Koopmans, P. V. Santos, R. B. Bergmann, and B. Richards, Appl. Phys. Lett. **69**, 3719 (1996).

[7] E. Hartfield and B.J. Thompson, in *Handbook of Optics*, edited by W. G. Driscoll and W. Vaughan (McGraw-Hill, New York, 1978), Chap. 17.

[8] J. F. Nye, *Physical Properties of Crystals* (Oxford University Press, Oxford, 1976).

[9] B. N. Grechushnikov, in *Modern Crystallography IV, Physical Properties of Crystals*, edited by L. A. Shuvalov (Springer, Berlin, 1988), Chap. 7.

[10] N. Suzuki and K. Tada, Jpn. J. Appl. Phys., Part 1 **22**, 441 (1983).

[11] F. Canal, M. Grimsditch, and M. Cardona, Solid State Commun. **29**, 523 (1979).

[12] P. Renosi, J. Sapriel, and B. Djafari-Rouhani, in *Conference Proceedings of the Fifth International Conference on Indium Phosphide and Related Materials* (IEEE, New York, 1993), p. 592.

[13] U. Gerhardt, Phys. Rev. Lett. **15**, 401 (1965).
[14] F. H. Pollak and M. Cardona, Phys. Rev. **172**, 816 (1968).
[15] P. Etchegoin, J. Kircher, M. Cardona, and C. Grein, Phys. Rev. B **45**, 11 721 (1992).
[16] P. Etchegoin, J. Kircher, M. Cardona, C. Grein, and E. Bustarret, Phys. Rev. B **46**, 15 139 (1992).
[17] P. Etchegoin, J. Kircher, and M. Cardona, Phys. Rev. B **47**, 10 292 (1993).
[18] B. Koopmans, P.V. Santos, and M. Cardona (unpublished).
[19] J. Camassel, P. Merle, L. Bayo, and H. Mathieu, Phys. Rev. B **22**, 2020 (1980).
[20] A. Gavini and M. Cardona, Phys. Rev. B **1**, 672 (1970).
[21] Y. Chen, B. Gil, and H. Mathieu, Ann. Phys. (Paris) **12**, 109 (1987).
[22] R. A. Bendoryus and A. Y. Shileika, Fiz. Tekh. Poluprovodn. **6**, 1125 (1972) [Sov. Phys. Semicond. **6**, 1042 (1972)].
[23] T. Kobayashi, K. Aoki, and K. Yamamoto, Physica B **139 & 140B**, 537 (1986).
[24] H. Müller, R. Trommer, M. Cardona, and P. Vogl, Phys. Rev. B **21**, 4879 (1980).
[25] R. Zallen and W. Paul, Phys. Rev. **155**, 703 (1967).
[26] A. L. Edwards and H. G. Drickhamer, Phys. Rev. **122**, 1149 (1961).
[27] V. K. Bazhenov, A. M. Mutal, and V. I. Soloshenko, Fiz. Tekh. Poluprovodn. **9**, 1893 (1975) [Sov. Phys. Semicond. **9**, 1247 (1976)].
[28] A. Blacha, H. Presting, and M. Cardona, Phys. Status Solidi B **126**, 11 (1984).
[29] I. Gorczyca, N. E. Christensen, and M. Alouani, Phys. Rev. B **39**, 7705 (1989).
[30] K. J. Chang, S. Froyen, and M. L. Cohen, Solid State Commun. **50**, 105 (1984).
[31] M. Cardona and N. E. Christensen, Phys. Rev. B **35**, 6182 (1987).
[32] P. E. Van Camp, V. E. Van Doren, and J. T. Devreese, Phys. Rev. B **41**, 1598 (1990).
[33] C. Priester, G. Allan, and M. Lannoo, Phys. Rev. B **37**, 8519 (1988).
[34] M. Silver, W. Batty, A. Ghiti, and E. P. O'Reilly, Phys. Rev. B **46**, 6781 (1992).
[35] J. Kircher, W. Böhringer, W. Dietrich, H. Hirt, P. Etchegoin, and M. Cardona, Rev. Sci. Instrum. **63**, 3733 (1992).
[36] M. Garriga, Ph.D. thesis, Universität Stuttgart, 1990.
[37] D. E. Aspnes and A. A. Studna, Rev. Sci. Instrum. **49**, 291 (1978).
[38] R. M. A. Azzam and N. M. Bashara, *Ellipsometry and Polarized Light* (North-Holland, Amsterdam, 1977).
[39] D. E. Aspnes, J. Opt. Soc. Am. **70**, 1275 (1980).
[40] C. M. Herzinger, P. G. Snyder, B. Johs, and J. A. Wollam, J. Appl. Phys. **77**, 1715 (1995).
[41] D. E. Aspnes and A. A. Studna, Phys. Rev. B **27**, 985 (1983).
[42] P. V. Santos, N. Esser, J. Groenen, M. Cardona, W. G. Schmidt, and F. Bechstedt, Phys. Rev. B **52**, 17 379 (1995).
[43] S. Zollner, Appl. Phys. Lett. **63**, 2523 (1993).
[44] D. E. Aspnes, in *Optical Properties of Solids, Vol. 2*, edited by M. Balkanski (North-Holland, Amsterdam, 1979), p. 109.
[45] S. M. Kelso, D. E. Aspnes, M. A. Pollack, and R. E. Nahory, Phys. Rev. B **26**, 6669 (1982).
[46] M. Erman, J. P. Andre, and J. LeBris, J. Appl. Phys. **59**, 2019 (1986).
[47] P. Lautenschlager, M. Garriga, and M. Cardona, Phys. Rev. B **36**, 4813 (1987).
[48] J. E. Rowe, F. H. Pollak, and M. Cardona, Phys. Rev. Lett. **22**, 933 (1969).
[49] F. H. Pollak, Surf. Sci. **37**, 863 (1973).
[50] M. Chandrapal and F. H. Pollak, Solid State Commun. **18**, 1263 (1976).
[51] M. Chandrasekhar and F. H. Pollak, Phys. Rev. B **15**, 2127 (1977).
[52] R. F. S. Hearmon, in *Numerical Data and Functional Relationship in Science and Technology*, Landolt-Börnstein, edited by K.-H. Hellwege and A. M. Hellwege, New Series, Group III, Vol. 11 (Springer-Verlag, Berlin, 1979), p. 27.
[53] P. Etchegoin, Ph.D. thesis, Universität Stuttgart, 1994.
[54] D. D. Sell and E. O. Kane, Phys. Rev. **185**, 1103 (1969).
[55] M. I. Alonso and M. Cardona, Phys. Rev. B **37**, 10 107 (1988).
[56] P. Vogl, H. Hjalmarson, and J. Dow, J. Phys. Chem. Solids **44**, 365 (1983).
[57] M. L. Cohen and J. R. Chelikowsky, *Electronic Structure and Optical Properties of Semiconductors* (Springer-Verlag, Heidelberg, 1988).
[58] L. C. Lew Yan Voon and L. R. Ram-Mohan, Phys. Rev. B **47**, 15 500 (1993).
[59] M. Cardona, Phys. Rev. B **15**, 5999 (1977).
[60] W. A. Harrison, *Electronic Structure and the Properties of Solids* (Dover Publications, New York, 1989).
[61] L. Kleinman, Phys. Rev. **128**, 2614 (1962).
[62] R. Martin, Phys. Rev. B **1**, 4005 (1970).
[63] G. Theodorou and G. Tsegas, Phys. Rev. B **56**, 9512 (1997).
[64] H. Presting, Ph.D. thesis, Universität Stuttgart, 1985.
[65] D. J. Chadi, Phys. Rev. B **16**, 790 (1977).